Crystal structure, lattice vibrations, and superconductivity of LaO_{1−x}F_{x}BiS_{2}

J. Lee, M. B. Stone, A. Huq, T. Yildirim, G. Ehlers, Y. Mizuguchi, O. Miura, Y. Takano, K. Deguchi, S. Demura, and S.-H. Lee

Phys. Rev. B **87**, 205134 — Published 24 May 2013

DOI: 10.1103/PhysRevB.87.205134

Crystal Structure, Lattice Vibrations, and Superconductivity of $LaO_{1-x}F_xBiS_2$

J. Lee[1], M. B. Stone[2], A. Huq[3], T. Yildirim[4], G. Ehlers[2], Y. Mizuguchi[5,6], O. Miura[5], Y. Takano[6], K. Deguchi[6], S. Demura[6], and S.-H. Lee[1]

[1]*Department of Physics, University of Virginia, Charlottesville, VA 22904, USA*

[2]*Quantum Condensed Matter Division, Oak Ridge National Laboratory, Oak Ridge, Tennessee 37831-6393, USA*

[3]*Chemical and Engineering Materials Division, Oak Ridge National Laboratory, Oak Ridge, Tennessee 37831-6393, USA*

[4]*NIST Center for Neutron Research, National Institute of Standards and Technology, Gaithersburg, Maryland 20899, USA*

[5]*Department of Electrical and Electronic Engineering, Tokyo Metropolitan University, 1-1, Minami-osawa, Hachioji, 192-0397, Japan and*

[6]*National Institute for Materials Science, 1-2-1, Sengen, Tsukuba, 305-0047, Japan*

(Dated: April 24, 2013)

Neutron scattering measurements have been performed on polycrystalline samples of the newly discovered layered superconductor $LaO_{0.5}F_{0.5}BiS_2$, and its nonsuperconducting parent compound $LaOBiS_2$. The crystal structures and vibrational modes have been examined. Bragg peaks from the superconducting sample exhibit pronounced broadening compared to those from the nonsuperconducting one. In the inelastic measurements, a large difference in the high energy phonon modes was observed upon F doping. Alternatively, the low energy modes remain almost unchanged between non-superconducting and superconducting states either by F-doping or by cooling through the transition temperature. Using density functional perturbation theory we identify the phonon modes, and estimate the phonon density of states. We compare these calculations to the current measurements and other theoretical studies of this new superconducting material.

PACS numbers: 61.05.F-,63.20.dk,74.25.Kc,78.70.Nx

Superconductivity has been fascinating scientists for more than a century[1]. Several families of superconducting (SC) materials and mechanisms have been found and proposed: notably BCS superconductors where superconductivity is mediated by phonons, i.e. lattice vibrations, and unconventional superconductors whose superconductivity is yet to be fully understood. Many materials that belong to the latter category have layered crystal structures with low dimensionality. The cuprates with CuO_2 layers and the Fe-based superconductors with Fe-An (An: pnictogen or chalcogen anion) layers are two extensively studied examples[2–4]. Very recently, a new family of materials based on BiS_2 layers has been found to be SC at low temperatures: $Bi_4O_4(SO_4)_{1-x}$[5] and $LnO_{1-x}F_xBiS_2$ (Ln=La[6], Nd[7], Pr[8], Ce[9], and Yb[10]). The natural question that arises is whether the new Bi-based superconductors are conventional BCS superconductors or another family of non-BCS type superconductors yielding a new route for unconventional superconductivity.

Several theoretical studies have been reported especially for $LaO_{0.5}F_{0.5}BiS_2$ with currently the highest $T_c \approx$ 10.8 K among the Bi-superconductors. Theoretical consensus so far is that in $LaO_{0.5}F_{0.5}BiS_2$ the Fermi level crosses conduction bands yielding electron pockets[11–15]. From the quasi-one-dimensional (1d) nature of the conduction bands, these Fermi surfaces (FS) are nested by a (π,π) wave vector. The many body interactions and their relation to the superconductivity are, however, still controversial. A group of theories proposes that FS nesting, just as in the Fe-pnictides, makes electronic correlations a candidate for the pairing mechanism[12,16,17]. Alternatively, electron-phonon (e-ph) coupling constant (λ) calculations[14,15,18] find $\lambda \approx 0.85$ with $T_c \approx 11.3$ K, close to the experimentally found value, when the Coulomb parameter of the Allen-Dynes formula is 0.1. This suggests $LaO_{1-x}F_xBiS_2$ can be a conventional superconductor with strong e-ph coupling. Moreover, theories predict structural instabilities[14,18] which place this system in close proximity to competing ferroelectric and charge density wave (CDW) phases[18]. These instabilities are believed to be due to the anharmonic potential of the S ions lying on the same plane as the Bi ions. Just like the spin-density wave (SDW) instability in Fe-based superconductors, a CDW instability from imaginary frequency phonon modes at or around the M point, (π,π), is suggested to be essential to the superconductivity. The buckling of the BiS_2 plane, being related to the electronic structure and FS, was also suggested to be crucial in inducing superconductivity, and expected to decrease in the SC compound[18].

Experimentally, doping dependent structural measurements[19] suggest that the a lattice parameter is relevant to superconductivity. Both a and T_c increase with F substitution, and become maximal near optimal doping $x \approx 0.5$. The existence of electron pockets near the FS was experimentally shown by Hall effect measurements[20,21]. Other experimental studies to test the theoretical scenarios, however, are limited. Thus, detailed experimental studies of the crystal structure and lattice vibrations of non-SC and SC compounds are crucial in understanding the new Bi-superconductors.

Here we report neutron diffraction and inelastic neutron scattering measurements both on non-SC $LaOBiS_2$ and SC $LaO_{0.5}F_{0.5}BiS_2$ to investigate how the crystal structure and phonon density of states (PDOS) change as a function of F-doping and temperature. We also performed density functional linear response calculations

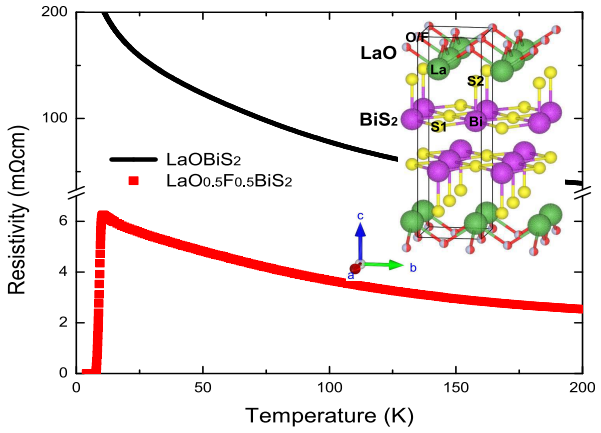

FIG. 1. (color online). Temperature dependent resistivities of $LaOBiS_2$ (black lines) and $LaO_{0.5}F_{0.5}BiS_2$ (red squares). The inset shows the crystal structure of $LaO_{1-x}F_xBiS_2$.

to identify the corresponding phonon modes. Experimentally obtained structural parameters are compared between the non-SC and SC compounds and with calculated values as well. Inelastic neutron scattering experiments show that while significant differences in the phonon spectrum were observed at higher energy transfers upon F doping, little change is observed in the low energy portion of the spectrum. On the other hand, the calculations predicts significant modisfication in the low energy spectrum where there is strong e-ph coupling, contrary to the experiment. Furthermore, we do not observe any meaningful change as a function of temperature in the phonon spectrum of the SC compound in the vicinity of T_c. The absence of phonon anomaly in either doping or temperature change suggests the e-ph coupling in this system could be much weaker than previously expected.

A 4.89 g polycrystalline sample of $LaOBiS_2$ was synthesized using the solid state reaction method under ambient pressure while a 0.89 g polycrystalline sample of $LaO_{0.5}F_{0.5}BiS_2$ was synthesized under high pressure at the NIMS, Tsukuba, Japan. Details concerning sample synthesis are described in Ref.[6,19]. Figure 1 shows the low-temperature resistivity of the parent and the F doped compound. $LaO_{0.5}F_{0.5}BiS_2$ exhibits a clear onset of SC transition at $T_c \approx 10.8$ K. Bulk superconductivity has been observed by a large diamagnetic signal below 8K in the magnetic susceptibility measurement [6,19]. Recent specific heat measurement also confirms that the superconductivity in this sample is bulk in nature [10].

Neutron scattering measurements were performed at the Spallation Neutron Source (SNS) using the POWGEN diffractometer, the wide angular range chopper spectrometer (ARCS), and the Cold Neutron Chopper Spectrometer (CNCS). Samples were loaded into vanadium (at POWGEN and CNCS), or aluminum (at ARCS) cans with a He atmosphere and mounted to the closed cycle refrigerator (at POWGEN and ARCS) or liquid helium cryostat (at CNCS). Neutron diffraction data were collected using a wavelength band to cover a wide range of d spacing from 0.55 to 4.12 Å at POWGEN[22]. Inelastic neutron scattering (INS) measurements were performed at ARCS[23] with monochromatic neutrons of incident energies $E_i = 40$ and 80 meV. For improved resolution at low energy transfers, INS measurements were performed at CNCS[24] with $E_i = 25$ meV. All the INS data presented here are corrected for background by subtraction of an empty can measurement.

The phonon calculations were performed using QUANTUM-ESPRESSO[25] with ultrasoft pseudopotentials. The generalized gradient approximation (GGA) of Perdew-Burke-Ernzerhof[26] was used for the exchange correlation potential. A $20 \times 20 \times 6$ regular grid over the irreducible Brillouin Zone was used for the self-consistent calculation of the F doped and parent compound. A plane wave energy cutoff of 60 Ry and charge density energy cutoff of 480 Ry were used for both materials. A manual check of convergence for grid density, energy cutoff, and lattice parameter values was performed. In Appendix C we list the phonon energies at M=$(\pi, \pi, 0)$ for five different models, indicating that our calculations are well converged. To simulate the half doping in the SC sample, we replace oxygen at one of the $2a$ Wyckoff sites with F in an ordered fashion. In order to test the effect of the (O/F) ordering on the buckling of BiS_2 plane, we also repeated calculations using a system with charge-doping without actual F-substition. We obtained similar results as shown in Appendix D. The phonon DOS is calculated using the eigen-vectors from the linear response calculations. The negative energy modes are excluded in DOS calculations. However, due to very limited number of negative energy modes, we do not expect significant contribution from them to DOS. The powder-averaged phonon DOS is calcululated using a 20x20x8 q-grid based on the linear response calculations of the dynamical matrix over 4x4x2 grid.

The detailed crystal structure for the parent compound, $LaOBiS_2$, is first reported in this paper. Figure 2(a) shows neutron diffraction data and Rietveld refinements obtained from this sample. The nuclear Bragg peaks are instrumental resolution limited indicating good crystallinity. The data for the parent compound are well reproduced by the $P4/nmm$ space group with structural parameters and goodness of fit listed in Table I. We determine the crystal structure, as shown in the inset of Fig. 1, to be similar to that found by the preliminary x-ray scattering measurements on the doped compound[6,19]. The system has a layered structure where BiS_2 bilayers are well seperated by $La_2(O,F)_2$ blocking layers. The Bi ions form a square lattice just as the Cu and Fe ions do in the cuprates and Fe-based superconductors, respectively. There are two distinct Wyckoff sites for the sulfur ions, S_1 and S_2. While S_1 ions reside nearly on the same plane as the Bi square lattice with some buckling, the S_2 ions are just above or below the Bi ions.

On the other hand, for the SC $LaO_{0.5}F_{0.5}BiS_2$ most of the nuclear Bragg peaks are broader than instrumental resolution (Fig. 2(b)), indicating imperfect crystallinity.

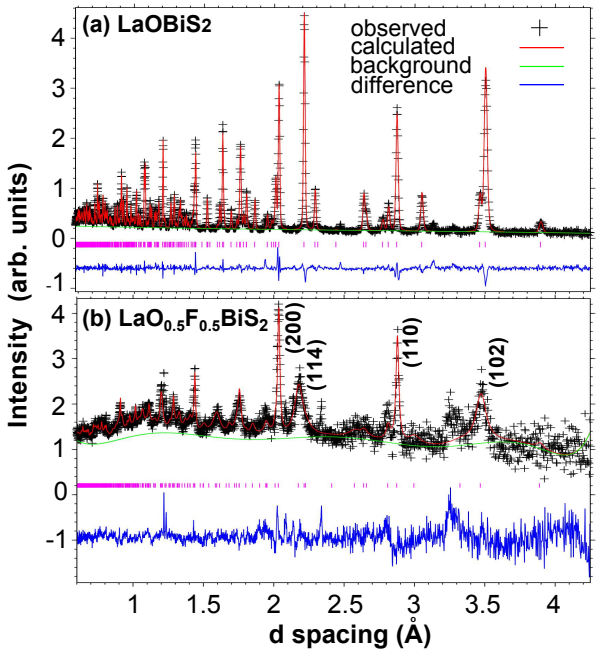

FIG. 2. (color online). Neutron powder diffraction data obtained from (a) $LaOBiS_2$, and (b) $LaO_{0.5}F_{0.5}BiS_2$ at 15K. Black crosses represent observed data. Red, green, and blue solid lines are the calculated intensity, estimated background, and difference between the observed and calculated intensity obtained by GSAS[27], respectively.

	Experiment	Calculation
LaOBiS2	Rwp = 0.074	
P4/nmm T=15K	χ^2 = 19.4	
a (Å)	4.05735(5)	4.03949
c (Å)	13.8402(3)	14.30361
c/a	3.41114(8)	3.54095
La 2c (0.5, 0, z)	0.0907(1)	0.0853
Bi 2c (0, 0.5, z)	0.3688(1)	0.3665
S_1 2c (0.5, 0, z)	0.3836(3)	0.3949
S_2 2c (0.5, 0, z)	0.8101(2)	0.8112
O 2a (0, 0, 0)	–	–
$\lvert z_{Bi} - z_{S1}\rvert / z_{Bi}$	4.01(8) (%)	7.75 (%)
$LaO_{0.5}F_{0.5}BiS_2$	wRp = 0.065	
P4/nmm T=15K	χ^2 = 3.43	
a (Å)	4.0651(3)	4.07989
c (Å)	13.293(7)	13.42520
c/a	3.2700(16)	3.2906
La 2c (0.5, 0, z)	0.1007(5)	0.1034
Bi 2c (0, 0.5, z)	0.3793(5)	0.3839
S_1 2c (0.5, 0, z)	0.362(2)	0.3840
S_2 2c (0.5, 0, z)	0.815(1)	0.8160
O 2a (0, 0, 0)	–	–
F 2a (0, 0, 0)	–	–
$\lvert z_{Bi} - z_{S1}\rvert / z_{Bi}$	4.5(5) (%)	0.0260 (%)

TABLE I. Refined structural parameters of $LaOBiS_2$ and $LaO_{0.5}F_{0.5}BiS_2$ obtained from neutron powder diffraction and calculated with structural optimization implemented in QUANTUM ESPRESSO. The quantity $\lvert z_{Bi} - z_{S1}\rvert / z_{Bi}$ characterizes the amount of buckling. wRp and χ^2 respectively are the weighted R factor and chi squared values from the structural refinements[27]. Though there are some unindexed peaks in the refinement, the weight percentage of impurities is small based upon their relative intensities. Numbers in parentheses here and throughout the manuscript correspond to one standard deviation in the mean value.

Similar broadening has been reported in prior X-ray measurements[6,19]. We note that the broad peaks have an asymmetric line-shape, characteristic of a low dimensional crystal ordering. The asymmetric broad peaks index with nonzero l values, while $l = 0$ Bragg peaks are considerably sharper and more symmetric. This is clearly seen in Fig. 2(b), for example, where the (200) peak at $d = 2.03$ Å and the (110) peak at $d = 2.87$ Å are sharp while the (114) peak at $d = 2.17$ Å and the (102) peak at $d = 3.47$ Å are broad and asymmetric. This suggests that strain may be induced along the c-axis due to a random replacement of the F ions at O sites. As a result, the La(O,F) planes are not well ordered along the c-axis. The solid line in Fig. 2(b) is our best refinement to the data, where a phenomenological model of anisotropic broadening has been used[28]. Details of the refinement is provided in the Appendix. This coarsely reproduces the diffraction data and allows for reasonable determination of the structural parameters, summarized in Table I.

We find upon F doping, the lattice elongates along a by $\approx 0.2\%$ while it contracts along c by $\approx 4.1\%$, consistent with previous x-ray results[19]. This F-doping induced lattice change is reproduced by our calculations although the rates are different. The buckling of the BiS_2 plane is found to slightly increase as shown in Table I. This contradicts a prior theoretical prediction[18] as well as the structure optimization calculations presented here. The atomic positions in the superconducting sample, however, should be considered with care due to the large noise in the data. We note that although there is additional broadening in the superconducting sample diffraction data, the refinement converges to reliable values. Further work with additional or improved samples may be able to provide better accuracy.

We note that there are discrepancies between experimental and calculated structural parameters. First, there is a large difference in the interlayer distance: the optimized interlayer distance is larger than the experimental one, especially in the parent compound. This becomes more clear if we compare the c/a ratio as in the Table I. We also observe in *both* compounds a large discrepancy in the z position of the S_1 atom between experimental and theoretical values. The discrepancy in the z position of the S_1 atom was regarded as a sign of a possible structural instability in this system[18]. This deviation seems to become larger with F doping. According to frozen phonon calculations, the instability at or near the M point can reduce the symmetry of the F doped compound statically to $P222_1$[18], the CDW phase, or P-4m2[15]. This potential structural transition, however, could not be experimentally confirmed due to the Bragg peak broadening.

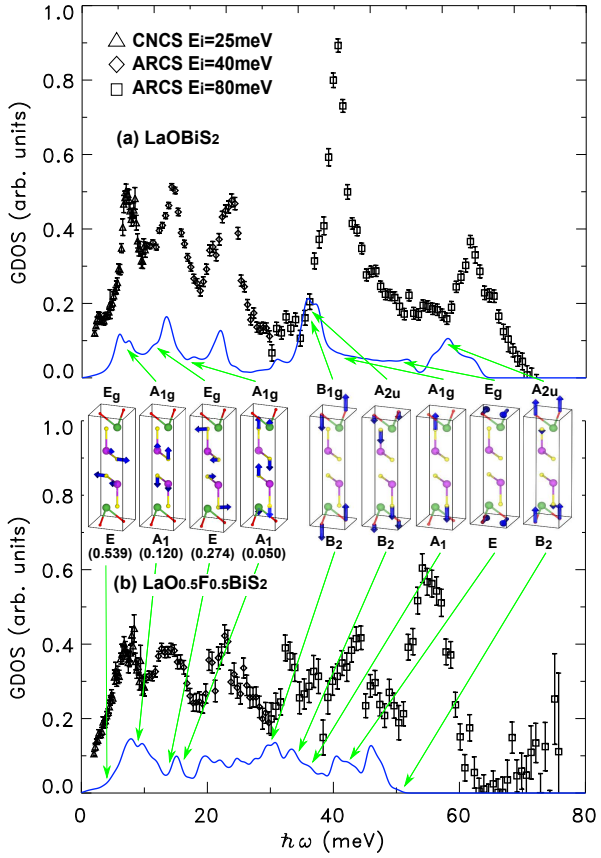

FIG. 3. (color online). GDOS as a function of $\hbar\omega$ for the (a) parent non-SC and (b) F substituted SC compound. Black symbols are the experimental data; blue solid lines are the calculated GDOS scaled for comparison. Three measurements have been combined: below 10 meV are from CNCS $E_i = 25$ meV, between 10 and 30 meV from ARCS $E_i = 40$ meV, and above 30 meV from ARCS $E_i = 80$ meV. To obtain the GDOS, the neutron scattering intensities were averaged over momentum transfers of [3, 6] Å^{-1}, [4, 7] Å^{-1}, and [3, 8.5] Å^{-1}, respectively. The phonon modes at the Γ point are shown in the inset with their symmetries for the parent (above) and SC (below) compound. Atoms are shown with the same colors as in Fig. 1, and their relative displacements are represented with thick blue arrows. The left four figures in the inset are the vibrational modes that are theoretically expected to have the large e-ph couplings, with each λ shown in parentheses. For the first mode shown here, the corresponding energy becomes negative (−2.9 meV) in the parent compound. For doublet modes, only one of the two orthogonal modes is shown.

To examine if the pairing mechanism of the superconductivity is phononic, we have performed INS measurements to obtain the neutron weighted generalized PDOS (GDOS). Figure 3 shows the GDOS as a function of energy transfer, $\hbar\omega$, for the two compounds at $T = 5$ K. Details of the data treatment are in the Appendix. For the non-SC $LaOBiS_2$, (Fig. 3(a)), there are well-defined phonon modes over a wide range of $\hbar\omega$ up to 70 meV. At least five prominent bands of lattice vibrations are present at 7.7(2), 14.2(1), 22.9(2), 40.4(1), and 61.8(4) meV. Upon F doping, as shown in Fig. 3 (b), the phonon modes at higher energies change significantly. All the vibrational modes become broader than their corresponding modes of $LaOBiS_2$. Furthermore, the top of the band softens in energy from 61.8(4) to 55.2(1) meV, and the sharp 40 meV peak significantly weakens. Conversely, the first two low energy peaks remain similar to those of the parent compound even though they broaden.

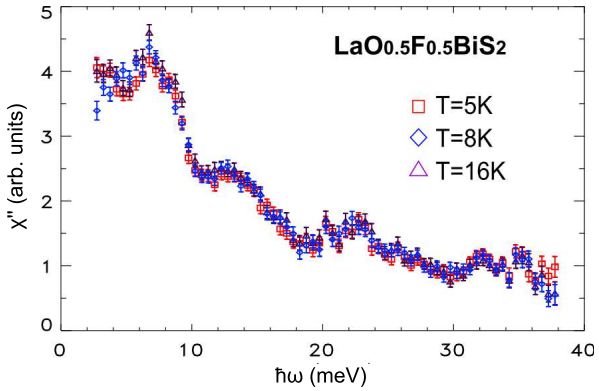

FIG. 4. (color online). Temperature dependence of the dynamical susceptibility. The data have been measured at ARCS with $E_i = 40$ meV, and integrated over Q = [4, 7] Å^{-1}.

Our calculated GDOS are shown as solid lines in Fig. 3. For the non-SC sample, it reproduces the observed prominent phonon modes reasonably well. Our calculations at the zone center show that the 40 and 62 meV bands are mainly due to vibrations of light ions. For example, in the inset of Fig. 3, the last 5 figures show the high energy vibration modes. These modes mostly involve O and/or S_2 vibrations. The intermediate energy modes around 13 and 23 meV are mainly due to S_1 and/or S_2 vibrations, while the low energy modes below ≈ 10 meV are due to the vibrations of the BiS_2 and/or LaO layers. Our calculations at the zone center also yield imaginary frequency unstable phonon modes involving vibrations of the BiS_2 layer, which was previously reported to be the sign of anharmonic ferroelectric soft phonons[18]. We list the calculated modes at the zone center in detail in the Appendix.

For the SC-sample, the calculated GDOS reproduces the features occurring at large $\hbar\omega$ (albeit shifted in energy); the broadening of high energy peaks, reduction of the sharp 40 meV peak, and softening of the highest energy O/F vibration modes. These changes can be partially understood as being due to the high energy O modes being shifted because of substitution with heavier F ions. This, however, fails to explain the low energy data. According to the calculation, solid lines in Fig. 3, most of the e-ph coupling comes from the low energy modes below ≈ 20 meV, and as such this is where we expect meaningful changes of the GDOS relevant to the superconductivity to occur. While the theory predicts considerable re-distribution of GDOS in this low energy

region, we do not observe any such change in the measured spectrum upon F doping.

To further probe for a phonon anomaly associated with superconductivity, we also examine the temperature dependence of the dynamical susceptibility, $\chi^{''}(\omega)$, of the SC $LaO_{0.5}F_{0.5}BiS_2$. Figure 4 shows $\chi^{''}(\omega)$ at three different temperatures spanning $T_c \approx 10.8$ K. Our experimental data show that $\chi^{''}(\omega)$ does not change within the experimental errors when the system transits from the normal to SC state. This suggests that, if it exists, the possible e-ph coupling in this material is much weaker than theoretically expected. We caution however that further detailed studies with a single crystal would be necessary to reach a more concrete conclusion in this regard.

In summary, our neutron powder diffraction data reveals the crystal structure of non-SC $LaOBiS_2$ and SC $LaO_{0.5}F_{0.5}BiS_2$. Large broadening of the Bragg peaks has been observed in the SC compound. In both compounds, discrepancies between experimental and calculated structural parameters have been observed, which suggest inherent structural instabilities in these systems. Furthermore, it was theoretically predicted that, in the SC phase, a significant change in the phonon density of states at low energies would occur due to a possible large e-ph coupling. Our inelastic neutron scattering data, however, yield no considerable change in the low energy phonon modes as the system becomes SC either by F-doping or by cooling through the superconducting transition. Our results should provide important constraints on future theoretical works examining these new Bi-based superconductors.

These research activities at UVA and ORNL's Spallation Neutron Source were sponsored by the Division of Materials Sciences and Engineering, Basic Energy Sciences (BES), US Department of Energy (DOE) under Award No. DE-FG02-10ER46384, and by the Scientific User Facilities Division, respectively.

Appendix A: Refinement of neutron diffraction data

To describe the neutron diffraction pattern of $LaO_{0.5}F_{0.5}BiS_2$, a phenomenological model of anisotropic broadening with multi-dimensional distribution of lattice metrics[28] has been used. In this model, the d spacing of Miller index is defined by

$$1/d^2 = M_{hkl} = \alpha_1 h^2 + \alpha_2 k^2 + \alpha_3 l^2 + \alpha_4 kl + \alpha_5 hl + \alpha_6 hk. \tag{A1}$$

The local variance of the d-spacing, or M_{hkl}, can be related to the line broadening, and can be expressed as

$$\sigma(M_{hkl}) = \sum_{i,j} C_{i,j} \frac{\partial M}{\partial \alpha_i} \frac{\partial M}{\partial \alpha_j} = \sum_{HKL} S_{HKL} h^H k^K l^L \tag{A2}$$

where $C_{i,j} = \langle (\alpha_i - \langle \alpha_i \rangle)(\alpha_j - \langle \alpha_j \rangle) \rangle$ is the covariance matrix of Gaussian distribution, and S_{HKL} is defined for H+K+L=4. Given the tetragonal crystal system, the possible non zero anisotropic strain parameters are S_{400}=S_{040}, S_{202}=S_{002}, S_{004}, and S_{220}, whose refined parameters are summarized in the Table II.

S_{400}	S_{004}	S_{220}	S_{202}
5.767E+01	6.083E+00	4.025E+01	1.546E+02
(1.140E+01)	(1.642E+00)	(1.059E+01)	(1.036E+01)

TABLE II. The anisotropic phenomenological strain parameter used to fit the diffraction pattern in the F substituted compound, $LaOFBiS_2$. The numbers in the parentheses represent estimated error.

	χ^2	R_{wp}	R_{exp}	B-R_{wp}	B-R_{exp}
$LaOFBiS_2$	19.4	0.074	0.017	0.074	0.017
$LaO_{0.5}F_{0.5}BiS_2$	3.43	0.065	0.035	0.084	0.045

TABLE III. The goodness of the fit for both samples. Rwp and Rexp follow the definition used in the GSAS[27] program, and B-R_{wp} and B-R_{exp} are R factors calculated for the Bragg peaks only.

We also provide a more comprehensive characterization of the goodness of the fit in the Table III. Though the χ^2 and Rwp are smaller for the SC compound, it is mainly due to the poor data statistics of this sample. Smaller overall Rexp, and Bragg R-factors also support that these effects are coming from the smaller intensities and larger relative errors in the SC compound.

Appendix B: Inelastic Neutron Scattering

The background corrected neutron scattering intensity is directly proportional to the double differential cross-section which is directly proportional in turn to the scattering function, $S(Q, \omega)$,

$$\frac{d^2\sigma}{d\Omega d\omega} \propto \frac{k_f}{k_i} S(\vec{Q}, \omega) \tag{B1}$$

where the k_i, and k_f are the incident and final neutron wave vectors. The scattering function for single phonon scattering in a polycrystalline sample can be written as,

$$S(Q,\omega) = \sum_i \sigma_i \frac{(\hbar Q)^2}{2m_i} exp(-2W_i) \frac{G_i(\omega)}{\omega} \langle n(\omega) + 1 \rangle \tag{B2}$$

where $\hbar Q$, $\hbar\omega$, $n(\omega)$, σ_i, m_i, $exp(-2W_i)$ and $G_i(\omega)$ are the momentum transferred to the sample, the energy transferred, the Bose thermal factor at a given temperature, total scattering cross section, mass, Debye-Waller factor, and the phonon density of states for the i^{th} atom in the unit cell, respectively. The bare PDOS can be written mathematically as,

Mode	displacement direction	atoms involved	symmetry	energy (meV)
1	a - b diagonal	S_1	E_u	-5.7
2	a + b diagonal			
3	(mainly) b	S_1	E_g	-2.9
4	(mainly) a			
5	(mainly) b	all	E_u	0
6	(mainly) a			
7	along c	all	A_{2u}	0
8	a - b diagonal	S_1	E_u	4.1
9	a + b diagonal			
10	(mainly) a	S_1	E_g	5.2
11	(mainly) b			
12	along c	BiS_2 layer	A_{1g}	7.8
13	along c	S_1	A_{2u}	8.4
14	a - b diagonal	S_2 and La	E_g	12.7
15	a + b diagonal			
16	out of plane	S_1	A_{1g}	15.9
17	out of plane	S_1	A_{2u}	16.0
18	(mainly) b	S_2	E_u	17.4
19	(mainly) a			
20	(mainly) b	S_2	E_g	17.9
21	(mainly) a			
22	out of plane	La	A_{1g}	22.9
23	(mainly) a	O	E_u	33.9
24	(mainly) b			
25	out of plane	O	A_{2u}	35.9
26	out of plane	S_2 and O	B_{1g}	37.7
27	out of plane	S_2	A_{1g}	42.7
28	(mainly) b	O	E_g	52.5
29	(mainly) a			
30	out of plane	O	A_{2u}	58.9

TABLE IV. The zone-center phonon modes of parent compound based on the fully optimized structure. The symmetry decomposition of the phonons are Γ = 4 A_{1g} + 5 A_{2u} + B_{1g} + 5 E_u + 5 E_g. The optimized lattice parameters are a=b=4.029 Å, c=14.21 Å, z(La) = 0.0859, z(Bi) = 0.3676, z(S) = 0.6054, z(S) = 0.1899.

Mode	displacement direction	atoms involved	symmetry	energy (meV)	el-ph λ
1	(mainly) b	all	E	0.0	0.0
2	(mainly) a				
3	out of plane	all	B_2	0.0	
4	(mainly) b	S_2	E	4.0	0.539
5	(mainly) a				
6	(mainly) b	BiS_2 layer	E	5.2	0.001
7	(mainly) a				
8	out of plane	S_1 and La	B_2	7.6	0.002
9	(mainly) a	S_2	E	8.5	0.007
10	(mainly) b				
11	out of plane	BiS_2 layer	A_1	9.0	0.120
12	mixed	S_2	E	13.8	0.274
13	mixed				
14	out of plane	S_1	A_1	16.1	0.050
15	out of plane	S_1	B_2	16.9	0.014
16	mixed	S_1 and S_2	E	18.8	0.006
17	mixed				
18	out of plane	S_1 and La	A_1	19.9	0.013
19	mixed	S_1	E	20.7	0.001
20	mixed				
21	mixed	S_1	E	22.6	0.0
22	mixed				
23	(mainly) b	O/F	E	29.4	0.0
24	(mainly) a				
25	out of plane	F	B_2	29.8	0.009
26	out of plane	O	B_2	33.9	0.001
27	out of plane	S_2	A_1	38.2	0.144
28	(mainly) b	O/F	E	42.1	0.0
29	(mainly) a				
30	out of plane	O and S_2	B_2	51.83	0.005

TABLE V. The zone-center phonon modes of the F substituted compound based on fully optimized structure. The symmetrey decomposition of the phonons are $\Gamma = 4\ A_1 + 6\ B_2 + 10$ E. The optimized lattice parameters are a=b=4.0697 Å, c=13.3433 Å, z(La) = 0.89602, z(Bi) = 0.38448, z(S) = 0.6163, z(S) = 0.18494. The calculated electron-phonon coupling constant (λ) for each phonon mode is also given.

$$F(\omega) = \frac{1}{N}\sum_{j,\vec{q}} \delta\left[\omega - \omega\left(j,\vec{q}\right)\right] \tag{B3}$$

where $\omega(j,\vec{q})$ is the frequencies of the phonon modes. We can see that the scattering function is related to the GDOS, $G(E)$, as,[29,30]

$$G(E) = \sum_i \frac{\sigma_i}{2m_i} e^{-2W_i(Q)} F_i(\omega) / \sum_i \frac{\sigma_i}{2m_i} e^{-2W_i(Q)}. \tag{B4}$$

The GDOS, therefore, reflects the PDOS while the intensity contribution from its components are weighted by the σ_i/m_i, which are 0.07, 0.26, 0.21, 0.04, 0.03 barn/amu for La, O, F, Bi, and S, respectively. It is clear that the effect from oxygen and fluorine will be prominent in the GDOS measured by neutron scattering, and the GDOS will be weighted to the higher frequency compared with the bare PDOS. In general, however, the peak positions are not very sensitive to this neutron scattering weighting factor. The incoherent approximation requires the scattering function to be averaged over a wide range of wave vector transfer, Q, unless the scattering is purely incoherent, so that the correlation between motions of distinct atoms cancels. For our measurement, the neutron scattering intensity was averaged over momentum of 3 $Å^{-1}$ to 6 $Å^{-1}$ for E_i = 25 meV, 4 $Å^{-1}$ to 7 $Å^{-1}$ for E_i = 40 meV, and 3 $Å^{-1}$ to 8.5 $Å^{-1}$ for E_i = 80 meV.

Since the above equation only applies for single phonon scattering, proper consideration of multiple scattering and multiphonon contributions is necessary. It is known that, in general, the correction from these factors produce only minor effects on the realistic PDOS, and in our case, constant background subtraction[31] was applied to remove linearly increasing GDOS intensity above the phonon cutoff energy. The contribution from elastic scattering has been also eliminated by removing the intensities below 2meV. The final GDOS has been normalized

Mod.	Sym.	Cal.1 60 Ry 600 Ry 18x18x8 opt.	Cal.2 60 Ry 600 Ry 8x8x8 opt.	Cal.3 40 Ry 480 Ry 18x18x8 opt.	Cal.4 40 Ry 480 Ry 8x8x8 opt.	Cal.5 40 Ry 480 Ry 8x8x8 exp.
ω_1	A_1	-105.1	-118.2	-91.8	-118.1	-118.8
ω_2	B_1	-102.1	-114.5	-88.7	-114.4	-114.6
ω_3	B_2	-82.6	-82.8	-72.5	-82.7	-72.0
ω_4	A_2	-79.6	-77.0	-70.1	-76.9	-65.5
$\omega_{5,6}$	E	67.2	66.2	68.5	67.4	58.0
$\omega_{7,8}$	E	68.2	68.7	69.3	69.7	64.4
ω_9	B_2	74.7	76.5	75.8	75.8	66.9
ω_{10}	A_2	75.7	76.5	76.7	75.9	68.2
ω_{11}	A_1	77.5	77.0	77.3	77.8	72.5
ω_{12}	B_1	77.6	77.8	77.6	78.6	72.5
ω_{13}	B_2	77.8	79.1	78.4	80.2	82.3
ω_{14}	A_2	123.5	123.4	123.7	123.6	124.5
$\omega_{15,16}$	E	132.1	129.4	132.9	129.4	101.6
ω_{17}	A_1	156.8	156.9	156.7	157.0	156.8
ω_{18}	B_1	172.4	172.6	172.3	172.5	173.2
ω_{19}	A_2	185.3	184.3	186.6	185.3	196.2
ω_{20}	B_2	189.0	188.4	189.4	188.6	196.4
ω_{21}	A_1	193.4	193.0	193.5	192.9	199.7
ω_{22}	B_1	196.5	195.6	196.8	195.6	205.1
$\omega_{23,24}$	E	204.7	205.8	214.0	214.8	214.0
$\omega_{25,26}$	E	261.6	260.5	263.3	262.3	259.4
ω_{27}	A_2	263.8	264.0	272.2	272.4	271.5
ω_{28}	B_2	306.0	305.8	310.6	311.0	310.0
$\omega_{29,30}$	E	399.1	398.0	401.8	401.6	401.6

TABLE VI. The phonon modes at the $M(\pi,\pi,0)$ for $LaO_{0.5}F_{0.5}BiS_2$ calculated with different energy and charge density cutoff and k-point grid. All the atomic positions were optimized except the last raw (cal.5) which is calculated using experimental z-positions for the S atoms. We note that regadless of the deails of the calculations, we always get four negative energy modes. The mode energies are given in cm^{-1}.

for the integrated area over the whole energy range to become unity for both samples.

In Table IV and Table V, the phonon modes have been identified with their symmetry label together with the mode energies at the Gamma point. It also shows the ions involved and their vibrational direction. All the modes have either in plane or out of plane vibrational character.

Appendix C: Convergence Test of the Negative Energy Modes near M-point

In order to test the accuracy of our results, here we repeated the linear response phonon calculations at the M=$(\pi,\pi,0)$ point for $LaO_{0.5}F_{0.5}BiS_2$, using different energy and charge cutoff as well as different k-point grid. We also test if the negative energy modes are sensistive to the the z-values of the S-atoms used in the calculations. We repeated calculations using both optimized atomic positions and experimental positions. The results are summarized in Table.6. From this table, it is clear that our calculations are well converged since the phonon energies do not change much with different cutoff and k-grid point. The most importantly, we always get the negative energy modes, which has been attributed to charge density wave ordering[14,18].

Appendix D: Buckling versus F-Doping and Charge Doping

Here we discuss the buckling of the BiS_2 plane as a function of doping. We tested two models. In the first model, we approximate the F-doping by assuming a supercell structure of perfectly ordered O/F lattice. In the second model, we assume we have a perfect disorder of O/F and therefore the system can be simply modeled as charged system without actual F-doping. The buckling of the BiS_2 plane from both models is shown in Figure 5. We note that both models give the same behavior, i.e. the buckling decreases with doping. In the ordered 0/F model, the buckling vanishes completely at x=0.5 doping level while it is reduced down to 1% for the charged-model with O/F disorder. This indicates the importance of the nature of F-doping in real system. Since we did not observe significant decrease in the buckling of the BiS_2 plane and also the mode softening with doping is much smaller than calculated one, we think that the level of actual F-doping in our sample is not complete and probably very inhomogenous. This may explain some of the disagreement between experiment and calculations.

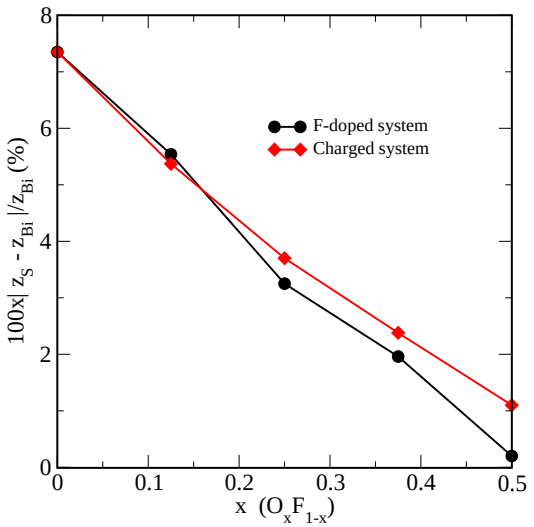

FIG. 5. (color online). The buckling, defined as $|z_{Bi} - z_{S_1}|/z_{Bi}$, as a function of doping. The doping effect is modeled as an ordered structure of (F/O) (black line) and as a disordered model where the system is treated with a net charge and without actual F-doping (red line). We note that both doping models give similar trend that the buckling of the BiS_2 plane decreases with doping level approaching to 0.5.

[1] H. K. Onnes, Commun. Phys. Lab. Univ. Leiden **12**, 120 (1911).
[2] P. Dai, J. Hu, and E. Dagotto, Nat. Phys. **8**, 709 (2012).
[3] M. A. Kastner, R. J. Birgeneau, G. Shirane, and Y. Endoh, Rev. Mod. Phys. **70**, 897 (1998).
[4] N. P. Armitage, P. Fournier, and R. L. Greene, Rev. Mod. Phys. **82**, 2521 (2010).
[5] Y. Mizuguchi, S. Demura, K. Deguchi, Y. Takano, H. Fujihisa, Y. Gotoh, H. Izawa, and O. Miura, Phys. Rev. B. **86**, 220510(R) (2012).
[6] Y. Mizuguchi, S. Demura, K. Deguchi, Y. Takano, H. Fujihisa, Y. Gotoh, H. Izawa, and O. Miura, J. Phys. Soc. Jap. **81**, 114725 (2012).
[7] S. Demura, Y. Mizuguchi, K. Deguchi, H. Okazaki, H. Hara, T. Watanabe, S. J. Denholme, M. Fujioka, T. Ozaki, H. Fujihisa, Y. Gotoh, O. Miura, T. Yamaguchi, H. Takeya, and Y. Takano, arXiv: 1207.5248.
[8] R. Jha, S. Kumar Singh, and V.P.S. Awana, J. Supercond. Nov. Magn. **26**, 499 (2013).
[9] J. Xing, S. Li, X. Ding, H. Yang, and H.-H. Wen, Phys. Rev. B **86**, 214518 (2012).
[10] D. Yazici, K. Huang, B. D. White, A. H. Chang, A. J. Friedman, and M. B. Maple, Philosophical Magazine **93**, 673 (2013); arXiv 1301.3932.
[11] H. Usui, K. Suzuki, and Kazuhiko Kuroki, Phys. Rev. B. **86**, 220501(R) (2012).
[12] T. Zhou and Z. D. Wang, J. Supercond. Nov. Magn. 10.1007/s10948-012-2073-4, (2012).
[13] V.P.S. Awana, A. Kumar, R. Jha, S. Kumar, J. Kumar, A. Pal, Shruti, J. Saha, and S. Patnaik, arXiv: 1207.6845.
[14] X. Wan, H.-C. Ding, S. Y. Savrasov, and C.-G. Duan, Phys. Rev. B **87**, 115124 (2013).
[15] B. Li, Z. W. Xing, and G. Q. Huang, Euro. Phys. Lett. **101**, 47002 (2013).
[16] S. L. Liu, arXiv: 1210.2154v1.
[17] G. B. Martins, A. Moreo and E. Dagotto, Phys. Rev. B. **87**, 081102(R) (2013).
[18] T. Yildirim, Phys. Rev. B. **87**, 020506(R) (2013).
[19] K. Deguchi, Y. Mizuguchi, S. Demura, H. Hara, T. Watanabe, S. J. Denholme, M. Fujioka, H. Okazaki, T. Ozaki, H. Takeya, T. Yamaguchi, O. Miura, and Y. Takano, Europhys. Lett. **101**, 17004 (2013).
[20] S. Li, H. Yang, J. Tao, X.n Ding, and H.-H. Wen, arXiv: 1207.4955v1.
[21] S. K. Singh, A. Kumar, B. Gahtori, S. Kirtan, G. Sharma, S. Patnaik, and V. P.S. Awana, J. Am. Chem. Soc. **134**, 16504 (2012).
[22] A. Huq, J. P. Hodges, O. Gourdon, L. Heroux, Zeitschrift fur Kristallographie Proceedings **1**, 127 (2011).
[23] D. L. Abernathy, M. B. Stone, M. J. Loguillo, M. S. Lucas, O. Delaire, X. Tang, J. Y.Y. Lin, B. Fultz, Rev. of Sci. Inst. **83**, 15114 (2012).
[24] G. Ehlers, A. A. Podlesnyak, J. L. Niedziela, E. B. Iverson, P. E. Sokol, Rev. of Sci. Inst. **82**, 85108 (2011).
[25] P. Giannozzi et al., J. Phys.: Condens. Matter, **21**, 395592 (2009).
[26] J. P. Perdew, K. Burke, and M. Ernzerhof, Phys. Rev. Lett. **77**, 3865 (1996).
[27] C. Larson and R. B. von Dreele, Los Alamos National Laboratory Tech. Report No. LAUR 86, (2000).
[28] Peter W. Stephens, J. Appl. Cryst. **32** , 281 (1999).
[29] S. W. Lovesey, Theory of Neutron Scattering from Condensed Matter Vol. 1 (Clarendon, Oxford, 1984).
[30] G. L. Squires, Introduction to the Theory of Thermal Neutron Scattering (Cambridge Univ. Press, 1978).
[31] V. F. Sears, E. C. Svensson, and B. M. Powell, Can. J. Phys. 73, 726 (1995).